Three-dimensional modelling and inversion of dc resistivity data incorporating topography – I. Modelling

Carsten Rücker,[1] Thomas Günther[2] and Klaus Spitzer[3]

[1]*Institute of Geophysics and Geology, University of Leipzig, Germany. E-mail: cruecker@uni-leipzig.de*
[2]*Leibniz Institute for Applied Geosciences, Hannover, Germany and*
[3]*Institute of Geophysics, University of Mining and Technology Freiberg, Germany*

SUMMARY

We present techniques for the efficient numerical computation of the electrical potential with finite element methods in 3-D and arbitrary topography. The crucial innovation is, firstly, the incorporation of unstructured tetrahedral meshes, which allow for efficient local mesh refinement and most flexible description of arbitrary model geometry. Secondly, by implementation of quadratic shape functions we achieve considerably more accurate results. Exploiting a secondary potential (SP) approach, meshes are downsized significantly in comparison with highly refined meshes for total potential calculation. However, the latter is necessary for the determination of the required primary potential in arbitrary model domains. To start with, we concentrate on the simulation of homogeneous models with different geometries at the surface and subsurface to quantify their influence. This results in a so-called geometry effect, which is not only a side effect but may be responsible for serious misinterpretations. Moreover, it represents the basis for treating heterogeneous conductivity models with the SP approach, which is especially promising for the inverse problem.

We address how the resulting system of equations is solved most efficiently using modern multifrontal direct solvers in conjunction with reordering strategies or rather traditional pre-conditioned conjugate gradient methods depending on the size of the problem. Furthermore, we present a reciprocity approach to estimate modelling errors and investigate to which degree the model discretization has to be refined to yield sufficiently accurate results.

Key words: electrical resistivity, finite element method, numerical techniques, topography, unstructured meshes.

1 INTRODUCTION

Direct current (dc) resistivity methods are widely used in geophysical near-surface investigations. The field technique is rather simple in its basic application although multielectrode systems have received a high technical standard nowadays. They are particularly applied if we want to achieve detailed information on the spatial distribution of electrical resistivities within the subsurface. 3-D structures, subsurface voids and surface topography are challenges we face if we want to calculate the geoelectrical response for realistic environments. The simulation software plays a decisive role in the data interpretation process and has to be capable of including all these features if we strive for solving the inverse problem in the end. This paper, therefore, focuses on the simulation or forward modelling routine and is basis of an inversion technique described by Günther *et al.* (2006, this issue).

The numerical calculation of the electric field started in the late 1960s using the techniques of integral equations (Dieter *et al.* 1969), finite element (FE) (Coggon 1971) and finite difference (FD) methods (Mufti 1976). A special variant basing on integral equations is the boundary element method (Okabe 1981). FD calculations in 3-D go back to Dey & Morrison (1979). They were the methods of choice throughout the 1980s and 1990s where several refinements were applied to them. Zhang *et al.* (1995), for example, presented improved boundary conditions for a more accurate potential approximation and Spitzer (1995), for example, introduced efficient pre-conditioned conjugate gradient solvers to decrease execution time.

By splitting up the total potential (TP) into a known reference potential of a background model and a secondary potential (SP) due to conductivity deviations from the background model, accurate numerical calculations of the SP can be carried out on moderate grids (Coggon 1971). This technique is known as singularity removal (Lowry *et al.* 1989) and was enhanced by Zhao & Yedlin (1996). However, it is used only for flat-earth problems with analytically known potentials.

The FD method is restricted to orthogonal grids, which limit its ability to reproduce non-orthogonal geometries. In recent years,
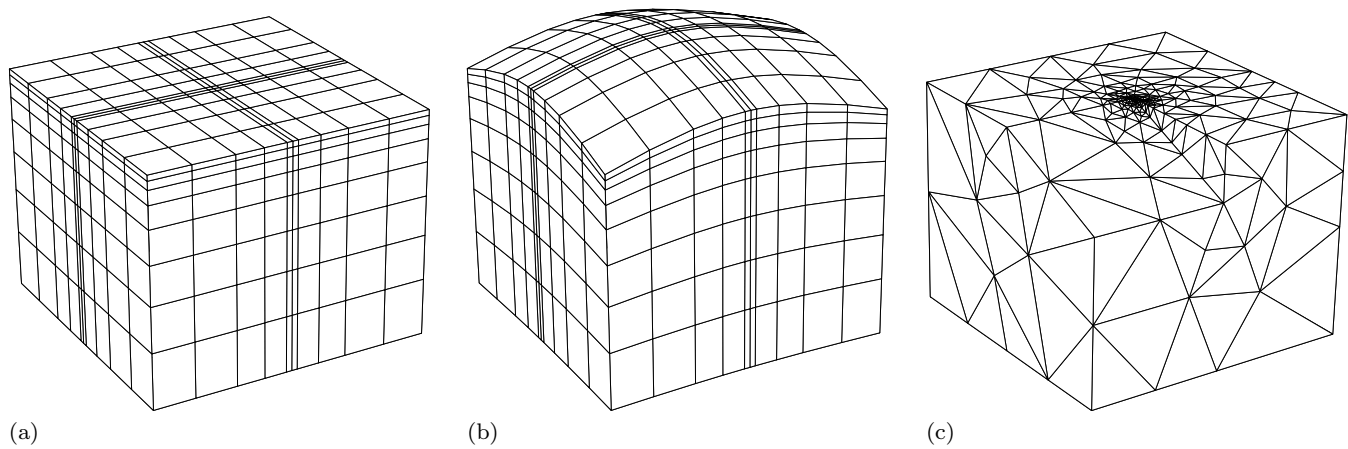
Figure 1. Different grid types: Orthogonal cuboid (a), non-orthogonal hexahedral (b) and unstructured tetrahedral (c) grid.

more and more FE approaches appeared, which are generally not subject to these drawbacks. Besides the aforementioned paper by Coggon (1971), FE formulations of the dc resistivity problem are described in Pridmore *et al.* (1980), Queralt *et al.* (1991), Li & Spitzer (2002), Zhou & Greenhalgh (2001) and Pain *et al.* (2003). Simulations with surface topography were presented in 2-D (Coggon 1971; Fox *et al.* 1980) and 3-D (Holcombe & Jiracek 1984; Sasaki 1994; Yi *et al.* 2001). However, the presented algorithms mainly work with block-oriented (structured) discretizations using hexahedral or tetrahedral elements and, thus, do not exploit the full power of the FE approach. Sasaki (1994) and Zhou & Greenhalgh (2001) use tetrahedral grids but since they are derived from bricks the approach is still block oriented.

Fig. 1 shows three possible grid types. (a) and (b) are regular types. The orthogonal hexahedral grid (a) is the one that is furthermost restricted with respect to geometry and local refinement. The local refinement of (b), a non-orthogonal regular hexahedral type, is still awkward and inefficient, but its geometrical adjustability is already increased. (c) shows an unstructured or irregular tetrahedral type, which is evidently the most flexible mesh in this regard. Particularly, refinement of regular grids results in an immoderately increased number of nodes, which consequently expands the numerical effort. Unstructured meshes are highly superior to the structured types with respect to these two points. They save computing resources and are, thus, one of the main issues of this paper.

We have implemented a C++ class library for FE problems that uses the non-commercial mesh generator TetGen (Si 2003) for the generation of unstructured tetrahedral meshes. Firstly, any model geometry and electrode layout can be described much more flexibly, for example, arbitrary electrode positions can be represented by prefixed nodes within the mesh. Secondly, the node distribution can be controlled on demand by refining the mesh locally in the vicinity of electrodes or at strong conductivity contrasts, that is, where strong gradients of the simulated potential require enhanced accuracy. In return, coarse grids are sufficient toward the boundaries to approximate the rather smooth fields appropriately.

As a result of any discretization technique, a sparse system of equations has to be solved for each current location. An overview on non-stationary iterative equation solvers for dc resistivity problems was given by Spitzer & Wurmstich (1999). They suggest conjugate gradient techniques with pre-conditioners. One very efficient, albeit memory consuming technique is obtained by an incomplete Cholesky (IC) decomposition (Kershaw 1978) as applied to dc mod-

elling by Dey & Morrison (1979) and Li & Spitzer (2002). In contrast to these iterative methods direct equation solvers have progressed rapidly in the recent years. Multifrontal decomposition methods going back to Duff *et al.* (1986) seem to suit best for problems with many right-hand sides, since the decomposition is done only once. The use of reordering techniques helps to limit the memory requirements for direct methods as well as for the IC pre-conditioner.

Accuracy in dc resistivity modelling is enhanced not only by grid refinement strategies but also by employing higher order basis functions in the FE approach. We show that a combination of both mesh refinement and quadratic shape functions yields most efficient solutions.

First we give an introduction to FE modelling, unstructured mesh generation and refinement. The homogeneous half-space is used to investigate how refinement strategies improve the results for the calculation of the TP. In the sequel, the conducting half-sphere is used to demonstrate the geometric flexibility of our approach and to apply the SP modelling. In two examples we show how complicated subsurface and surface geometry can be involved. We define a geometry effect to appraise the influence of any topography on dc resistivity measurements. Finally, we discuss computational aspects for the solution of the systems of equations.

2 FINITE ELEMENT FORWARD MODELLING

2.1 Calculation of the total potential

The boundary value problem is given by the equation of continuity with generalized boundary conditions:

$$\nabla \cdot (\sigma \nabla u) = -\nabla \cdot \mathbf{j} \text{ in } \Omega \subset \mathbb{R}^3, \tag{1a}$$

$$\sigma \left(\frac{\partial u}{\partial n} + \alpha u \right) = \mathbf{j} \cdot \mathbf{n} \text{ on } \Gamma = \Gamma_S \cup \Gamma_E, \tag{1b}$$

where $\sigma(x, y, z)$ is a given conductivity distribution in the ground, $\mathbf{j}$ the source current density and u the electrical potential, $\mathbf{n}$ denotes the outward normal on the corresponding boundary. We assume the current I being injected through point-like electrodes at the earth's surface Γ_S. Note that in the formulation above this may be done at Γ_S as well as within the modelling domain Ω, for example, using boreholes. For an electrode situated at $\mathbf{r}_s = (x_s, y_s, z_s)$ the source

term reads $\nabla \cdot \mathbf{j} = I\delta(\mathbf{r} - \mathbf{r}_s)$, where δ is Dirac's delta function. At Γ_S we impose Neumann conditions ($\alpha = 0$) to avoid current flow through the boundary. The other boundaries are treated with mixed boundary conditions after Dey & Morrison (1979) yielding $\alpha = \mathbf{n} \cdot \mathbf{r}/|\mathbf{r}|^2$. Note that we use the above formulation instead of the popular one because it is mathematically exact. Moreover it allows the node independent electrode positioning (see Appendix A).

The use of the weighted residual method (Zienkiewicz 1977) leads to the weak formulation of the boundary value problem (1),

$$\int_\Omega \sigma \cdot \nabla w \nabla u \, d\Omega + \int_\Gamma \sigma \alpha w u \, d\Gamma =$$
$$\int_\Omega w I\delta(\mathbf{r} - \mathbf{r}_s) \, d\Omega + \int_\Gamma w \mathbf{j} \cdot \mathbf{n} \, d\Gamma, \tag{2}$$

which has to be satisfied for a set of weighting functions w. The weak formulation allows a piecewise approximation of u but does not require the existence of a continuous second derivative.

The modelling domain is subdivided into disjunct elements. The integration on the individual elements leads to a system of linear equations $\mathbf{Au} = \mathbf{b}$ with the positive definite, symmetric and sparse matrix $\mathbf{A} \in \mathbb{R}^{N \times N}$, where N is the number of nodes, $\mathbf{u}$ is a vector containing the sought potentials and $\mathbf{b}$ is a vector of source terms. For details of the implementation of the equations with linear and quadratic shape functions see Appendix A.

2.2 Calculation of the secondary potential

The Dirac delta function δ in the source term of eq. (1a) leads to infinite potential gradients at the source position $\mathbf{r}_s$. Typically, this singularity is responsible for very poor numerical approximations of eq. (1a), particularly close to the electrode positions. The singularity can be removed according to a procedure described by Coggon (1971) for FE and Lowry *et al.* (1989) for FD. The potential u is split up into a primary and a secondary part $u = u_p + u_s$.

We yield the boundary value problem for the SP

$$\nabla \cdot (\sigma \nabla u_s) = \nabla \cdot ((\sigma_p - \sigma)\nabla u_p) \text{ in } \Omega \tag{3a}$$

$$\sigma \left(\frac{\partial u_s}{\partial n} + \alpha u_s \right) = (\sigma_p - \sigma) \left(\frac{\partial u_p}{\partial n} + \alpha u_p \right) \text{ on } \Gamma, \tag{3b}$$

where the singular current density $\mathbf{j}$ has vanished. However, the integral of eq. (3a) contains the gradient of the primary potential u_p. It is only guaranteed to be regular if the conductivity in the direct vicinity of the electrode equals σ_p. As already mentioned by Zhao & Yedlin (1996), for σ_p the local conductivity at the electrodes has to be chosen and not the mean conductivity as suggested by Lowry *et al.* (1989). Secondary sources appear where the conductivity deviates from σ_p.

Both left- and right-hand side differential operators are identical to that of the TP. By approximating the operators by matrices the system of equations can be written as

$$\mathbf{A}^\sigma \mathbf{u}_s = \mathbf{A}^{\sigma_p - \sigma} \mathbf{u}_p. \tag{4}$$

In order to avoid the assembling of $\mathbf{A}^{\sigma_p - \sigma}$ for each source conductivity σ_p we use the linearity of $\mathbf{A}$ by

$$\mathbf{A}^{\sigma_p - \sigma} \mathbf{u}_p = (\mathbf{A}^{\sigma_p} - \mathbf{A}^\sigma)\mathbf{u}_p = \mathbf{A}^1 \mathbf{u}_p \sigma_p - \mathbf{A}^\sigma \mathbf{u}_p. \tag{5}$$

Thus only one matrix $\mathbf{A}^1$ for a homogeneous conductivity of 1 has to be created additionally to $\mathbf{A}^\sigma$ for the whole forward calculation with many sources.

Note that, due to singularities in u_p, the right-hand side may only be approximated insufficiently using a coarse mesh. We, therefore, suggest numerical integration in the vicinity of the electrodes.

2.3 Solving the system of equations

The boundary conditions and, thus, the corresponding matrix entries depend on the source position. In order to avoid the intense reassembling of the coefficient matrix for each individual source of a multielectrode system we use a constant average source position for the boundary conditions, which is sufficiently accurate since the boundaries are generally far away from the sources. Hence, the matrix $\mathbf{A}$ is constant.

Both for the total and the secondary potential, a system of equations $\mathbf{Au}^l = \mathbf{b}^l$ has to be solved for each current source $l = 1$, ..., E, where E is the number of current sources. Thus, the system of equations is solved E times. Since the individual electrodes are used more than once, it is most efficient to calculate the potential for each single electrode and superpose the results. The matrix $\mathbf{A}$ is symmetric and sparse. With linear shape functions we generally obtain between 3 and 20 non-zero entries per row, with a mean of around 14.

For the solution of large, sparse systems of equations conjugate gradient methods (Hestenes & Stiefel 1952) prove to be very efficient (Spitzer & Wurmstich 1999). Their convergence can be significantly improved by the use of pre-conditioners. A very efficient pre-conditioner for many right-hand side vectors is achieved by IC factorization of $\mathbf{A}$, because the pre-conditioning process is done only once and the number of iterations per individual right-hand side vector is drastically reduced. There are two main variants of the incomplete factorization (Saad 1996; Zhou & Greenhalgh 2001). One restricts the non-zero elements to the sparsity structure of $\mathbf{A}$ (Dey & Morrison 1979; Li & Spitzer 2002; Wu *et al.* 2003). Another allows fill-in but neglects values smaller than a certain threshold (Saad 1996). We will address these as IC-nofill and IC-droptol in the following.

The conjugate gradient method using IC-droptol is somewhat a hybrid between iterative and direct methods. An IC decomposition with a threshold of 0 corresponds to a direct solver since the iteration is stopped after 1 iteration step. Consequently, direct methods are the matter of choice, if there is enough memory to save the complete Cholesky factor. In the past years multifrontal algorithms have been developed (Duff *et al.* 1986), which allow for efficient Cholesky decomposition. We use the C library TAUCS (Toledo *et al.* 2001), which provides direct and iterative solvers on the basis of multifrontal methods.

The fill-in produced by the (complete or incomplete) Cholesky factorization can be significantly diminished by reordering the matrix rows and columns. Historically, the oldest methods are Cuthill–McKee (CMK) and reverse Cuthill–McKee (RCM). A detailed description of the individual methods would go beyond this paper and can be found in mathematical literature (Saad 1996). Generally, three classes exist:

(i) Nested dissection (ND) is based on geometrical node separation (graph partitioning). A popular and very efficient implementation is METIS (Karypis & Kumar 1998).

(ii) Minimum degree (MD) methods try to reduce the neighbouring relations (degrees) of the nodes. Popular methods are multiple minimum degree (MMD) and approximate minimum degree (AMD) (Amestoy *et al.* 1996).

(iii) Minimum deficiency (MF) is a much more extensive technique which successively eliminates the nodes with minimal fill-in (Davis *et al.* 2000).

3 DISCRETIZATION AND ACCURACY

3.1 Mesh generation and refinement

An initial partitioning of the modelling domain often incorporates the given electrode layout as fixed nodes. However, an additional refinement has to be applied to obtain accurate forward calculations due to the singular potential at the electrodes. The existing approaches use block-oriented grids for both FD and FE calculations (Loke & Barker 1996; Wu *et al.* 2003; Yi *et al.* 2001). By introducing grid lines between electrodes the error is decreased. Using between two and four additional nodes they all end up in around 4 per cent relative error for a pole–pole configuration (Yi *et al.* 2001).

For a successive superposition of configurations with large geometric factors (such as dipole–dipole) a further refinement is required since the relative error is amplified by the geometric factor. However, since refining block-oriented grids always works in a global way, the number of nodes increases rapidly. One main advantage of unstructured meshes is the facilitation of refining grids within distinct regions. Thus in regions of varying potential gradients (close to electrodes) the mesh can be chosen very fine whereas toward the boundaries of the modelling domain the cell sizes grow.

One can distinguish between *a posteriori* and *a priori* refinement. For the former, the discretization depends on an error estimation procedure in the solution process, whereas for the latter, the information is introduced in advance. Since we know the critical regions, we choose the *a priori* type and enforce a locally fine mesh by introducing additional supporting nodes to the mesh generation process. In addition to the local node density, the approximation quality depends on the cell size growth (or prolongation) factor. This can mainly be controlled by the ratio of the tetrahedral edge lengths and the radius of the circumscribing sphere. Since sliver-shaped elements yield poor approximation properties, mesh generators try to minimize the radius-to-edge ratio. The maximum ratio throughout the mesh can be used as a global mesh quality control. We use TetGen (Si 2003), which tries to force all radius-to-edge ratios below a certain quality constraint. We choose a radius-to-edge ratio of 1.2 for all subsequent meshes, which, to our experience, provides sufficiently accurate results.

In order to create an unstructured mesh the domain has to be defined by points, polygons or faces, the so-called piecewise linear complex (PLC) (Shewchuk 1998). This includes the geometry of the domain and the electrode locations as well as the boundary. By introducing nodes and creating tetrahedral elements, the mesh generator creates the mesh of desired quality.

In the following we investigate local and global refinement techniques to find a trade-off between accuracy and computational effort. In addition to the spatial mesh refinement (h-method), we take into account the use of higher order shape functions (p-method).

3.2 Discretization for calculating the total potential

A uniform earth with a flat surface boundary offers the most simple analytical solution. We assume 21 electrodes in a straight line with 1 m spacing. The model boundaries are placed 5 km around the origin in order to minimize the effects of the boundary conditions. The first mesh created by the grid generator TetGen obtains 2047
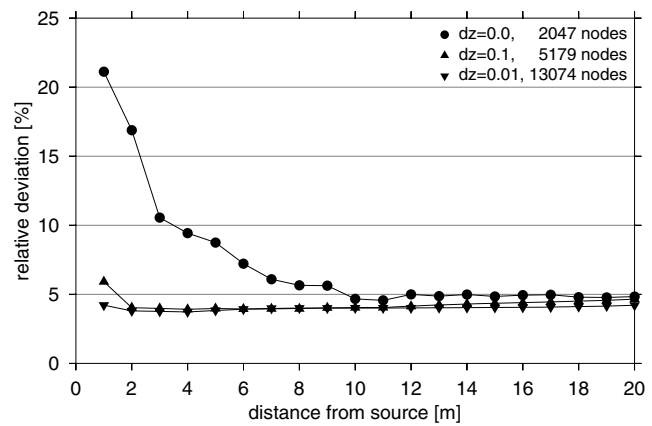
Figure 2. Relative deviation between analytical and numerical solutions of a pole–pole sounding for three meshes with increasing local refinement around the source electrode (total potential calculations).

nodes. Using the simulated potentials at the electrode locations we construct a pole–pole sounding curve for comparison with the analytical solution (upper curve in Fig. 2). In the vicinity of the source electrode we observe quite large errors, whereas with increasing distance the error stabilizes at around 5 per cent.

To diminish the large errors at the sources we increase the discretization density around the source node. By adding supporting points at a fixed depth dz below the electrodes the mesh generator is forced to apply a local refinement. In addition to the coarse unrefined mesh denoted by $dz = 0.0$ m (2047 nodes), Fig. 2 shows the results for the locally refined meshes denoted by $dz = 0.1$ m (5179 nodes) and $dz = 0.01$ m (13 074 nodes). The error is already almost constant for $dz = 0.1$ m. A further local refinement ($dz = 0.01$ m) yields only a negligible improvement. Therefore, we proceed using the mesh with the intermediate refinement ($dz = 0.1$ m).

Apparently, we need a global refinement to enhance the global error level of $\approx 4\%$. The simplest strategy is to bisect all tetrahedron edges such that each tetrahedron disintegrates into eight smaller ones. The number of nodes is increased approximately by a factor of 8 (38 533 nodes). Alternatively, we apply second order polynomials by replacing the 4-node tetrahedron by a 10-node tetrahedron, with a new node at each edge centre. Therefore, the resulting mesh nodes are identical to those of the h-refined mesh. Fig. 3 shows the relative deviations for the intermediate mesh of Fig. 2 of 5179 nodes (top), after a global refinement to 38 533 nodes (centre), and with the use of quadratic shape functions (bottom, also 38 533 nodes). By global refinement the error is halved to less than 2%, whereas quadratic shape functions yield errors around 0.1 per cent and below. The computational effort for solving the system of linear equations is nearly the same in both cases. However, we obtain significantly more accurate results by using the p-method.

First investigations show that the efficiency may not be improved any further by the use of even higher polynomial order. Therefore, we propose the use of locally refined meshes with quadratic shape functions for all calculations of the total potential.

3.3 Discretization for calculating the secondary potential

In order to show the flexibility of unstructured meshes we choose a spherical anomaly, which can hardly be discretized by block-oriented grids. The analytic solution for a conducting sphere is known (Large 1971; Zhdanov & Keller 1994). However, instead of a sphere in full-space, we consider a half-sphere at the
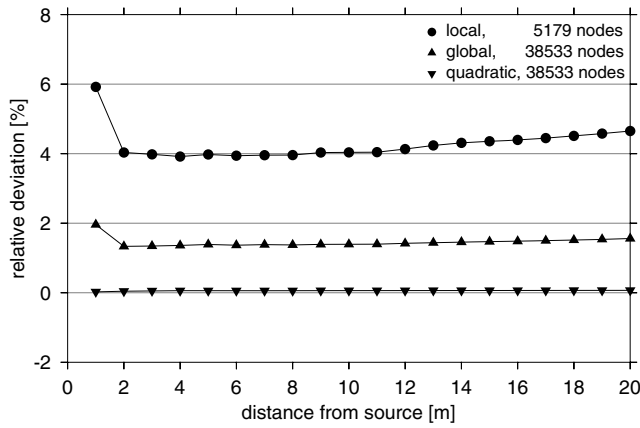
Figure 3. Relative deviation between the numerical and analytical solutions of a pole–pole sounding for different meshes and shape functions (total potential calculations).
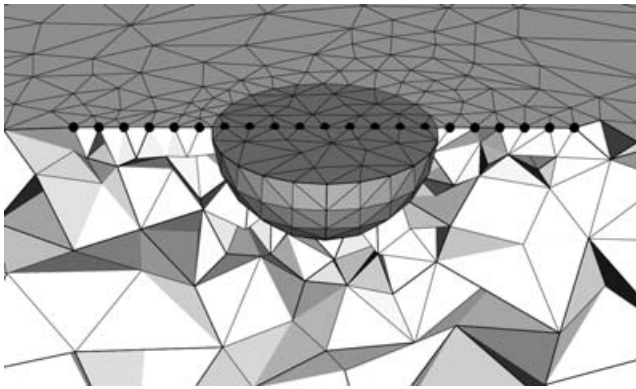
Figure 4. Section of the mesh used for the conducting half-sphere study. The dots denote electrode positions.

upper boundary of a half-space, on which electrodes are placed along a profile line. Since the half-space boundary is an axis of symmetry, the solution can easily be obtained by doubling the calculated potential values.

We expect the SP to be rather smooth so that we may start with a quite coarse mesh. Fig. 4 shows a section of the mesh. A half-sphere with a radius of 2.25 m is placed at the origin. We introduce a line of 21 electrodes from $x = -5$ m to $x = 5$ m with a spacing of 0.5 m as fixed nodes. Note that the electrodes can be placed independently of the nodes in general. We choose the model boundary to be 1000 m away from the origin in each direction. Using a radius-to-edge ratio of 1.2 a mesh of 1769 nodes has been generated on which the SP is simulated.

We assume the half-sphere to have a resistivity of 1 Ωm, whereas the half-space has $\rho_p = 10$ Ωm. We consider the source electrode at $\mathbf{r}_s = (-4; 0; 0)$ with the primary potential

$$u_p = \frac{I \rho_p}{2\pi |\mathbf{r} - \mathbf{r}_s|}.$$

Consequently, sources for the SP occur only within the half-sphere. The calculated potentials at the remaining electrodes are transformed into apparent resistivities using pole–pole geometric factors. In Fig. 5, the numerical results are compared to the analytical solution. Although the number of nodes is very small, the values agree very well. The relative deviation (right-hand side axis) stays below 1 per cent on the whole profile.
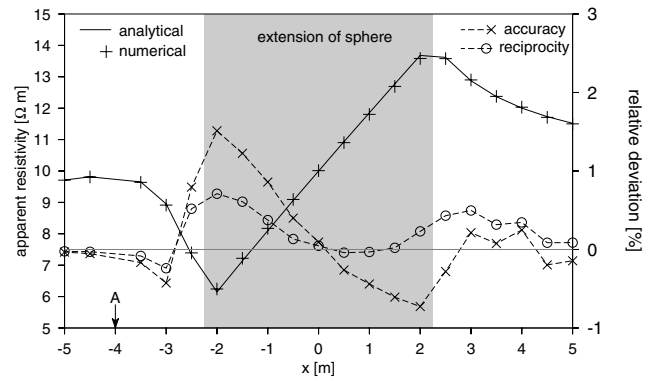
Figure 5. Apparent resistivity of a pole–pole configuration over a conducting half-sphere: comparison of analytical and numerical results using secondary potentials (A is the source position). The right-hand side axis denotes the relative deviation and the reciprocity measure r.

We now derive a measure of accuracy for cases where the analytical result is not available. Going back to the idea of Coggon (1971), Günther (2004) suggests to appraise the simulation results based on reciprocity. According to the reciprocity principle the measured potential remains constant if current and potential electrodes are interchanged. A deviation from this inevitably corresponds to simulation errors. As an indication for modelling errors we propose the reciprocity measure

$$r = 2 \frac{\rho_{\text{forward}}^a - \rho_{\text{reverse}}^a}{\rho_{\text{forward}}^a + \rho_{\text{reverse}}^a}, \tag{6}$$

where ρ_{forward}^a and ρ_{reverse}^a are the two simulated apparent resistivities with interchanged current and potential electrodes. In Fig. 5 we can see that in regions of increased errors the reciprocity measure r rises. To appraise a multielectrode simulation we regard the standard deviation and the maximum values of the individual reciprocity measures.

In order to compare the SP results with the solution for the TP, we have constructed a mesh for calculating the latter for the half-sphere model. The refinement factors have been chosen such that the accuracy is just as good as the one depicted in Fig. 5. With this proceeding we end up with 49 341 nodes, which is almost 30 times more than for the SP (1769 nodes).

Thus, the SP may be simulated on coarse meshes and with small computational effort. However, the primary potential can only be computed numerically if topography is present. In the following we concentrate on numerical simulations of a constant conductivity to obtain the primary potential for different model geometries.

4 MODELLING GEOMETRY EFFECTS

4.1 The geometry effect

Usually the measured electrical impedance $\Delta u/I$ is transformed into the apparent resistivity ρ_a by means of the geometric factor k. The latter is chosen such that the apparent resistivity equals the true resistivity in case of a homogeneous distribution. Clearly, the geometric factor depends on both electrode layout and the surface geometry. If the topography is non-trivial, k is unknown and can only be assessed numerically. We usually use an approximation k_a based on the half-space potentials for surface measurements and the full-space formula for subsurface measurements.

For any measurement, we want to discriminate between effects of the subsurface conductivity distribution and artefacts produced by using wrong geometric factors. Therefore, we define the geometry effect as the ratio of the voltage differences of the given geometry Δu and the approximation Δu_a. From the equality of the apparent resistivities we yield

$$t = \frac{\Delta u}{\Delta u_a} = \frac{k_a}{k}. \tag{7}$$

If any surface topography is present, we assign a homogeneous resistivity of $\rho = 1\,\Omega$m to the model and calculate the potential u numerically. Since ρ_a has to equal ρ we obtain the numerical geometric factor $k = I\rho/\Delta u$. t can be plotted for each datum to appraise geometry effects. With a value of $t = 1$ the measurement is not affected by topography. Values of $t > 1$ refer to increased apparent resistivities whereas values of $t < 1$ indicate a decrease.

4.2 A subsurface example

The following example originates from a dc resistivity survey inside a mining gallery to investigate its suitability as an repository for nuclear waste. The measurements were carried out at the side wall of the gallery. To interpret the measurements one is interested if half-space or full-space approximation can be used. The influence of the cavity finds expression in the value of the geometric factor k, which may be determined by simulating the electric potential for the gallery geometry within a homogeneous conductivity.

The gallery is 500 m long and has a 5×2 m cross-section. To minimize potential non-conformities from the outer boundary conditions we choose the model boundaries at a distance of 5 km from the gallery. A number of 50 electrodes with 1 m spacing are assumed at one side wall. Fig. 6 gives a view on the mesh used for the numerical calculations. The gallery itself is described by an inner surface with (no-flow) Neumann boundary conditions ($\alpha = 0$, see Section 2.1).

Alternatively, the problem could be solved by the approach of Queralt *et al.* (1991), since the resistivity distribution is 2-D and the array is parallel to the strike direction. However, the calculation is numerically instable as mentioned by the author. Furthermore, we search for a more general solution that is enable to involve real 3-D geometry.

In order to describe the model geometry and to approximate the TPs accurately, a large number of mesh nodes is necessary. With local mesh refinement at the vicinity of the electrodes and global quadratic shape functions the resulting mesh contains 128 169 nodes.
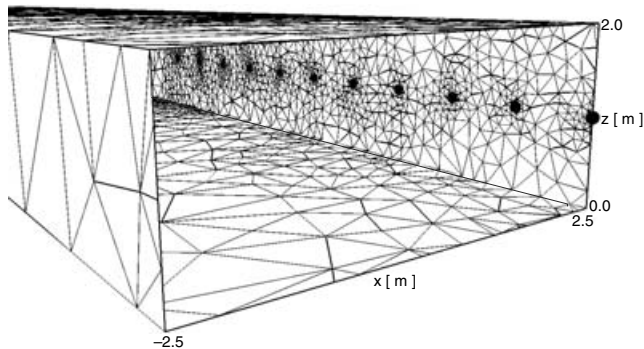
Figure 6. Surface mesh of the mining gallery model showing a part of the cavity. The dots denote electrode positions.
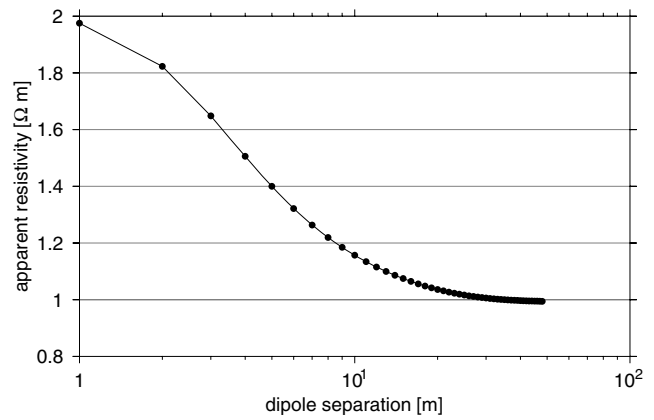
Figure 7. Full-space apparent resistivities of the dipole–dipole sounding as a function of the dipole separation.

A resistivity of 1 Ωm is assigned to the model. We used the full-space geometric factor to obtain the apparent resistivities. Fig. 7 shows the simulated ρ_a values as a function of the distance between transmitter and receiver dipole. Dipole length is the electrode spacing of 1 m.

The curve starts at values around 2 Ωm for small separations, which may be considered as half-space case and corresponds to a topography factor of $t = 2$. As the separation increases, the curve is tending more and more to 1 Ωm which is associated with the full-space case of $t = 1$. For practical applications, the geometry effect can be neglected if it falls below 10 per cent. In the case of the presented gallery this holds from a dipole separation of 15 m on. However, for small separations it has to be considered.

4.3 A complicated surface topography

To show a practical example with complicated surface topography we choose a structural investigation at Merapi volcano which was carried out in 1998 and 1999 (Friedel *et al.* 2000). Direct current measurements have been conducted at Merapi's northern, southern and western flanks which show a pronounced topography. The northern profile comprises 16 electrodes at ≈200 m, a total length of 2600 m, and altitude differences of up to 730 m. This profile is affected massively by the volcano topography.

First we need a surface mesh to apply the topography. We place the electrode positions and supporting points in 1 m distance. To satisfy boundary conditions and to include the whole volcano into the model, the boundary is chosen 10 km outside the electrodes. With the Triangle algorithm (Shewchuk 2002) we create a 2-D surface which is fine at the electrodes and coarse at the boundaries (Fig. 8a). It has only 4000 nodes, a regular mesh with similar refinement would obtain unlike more.

The TU Darmstadt provided the high-resolution topography data containing 300 000 points. To every node of the 2-D mesh an altitude is associated by interpolation. Together with the lower boundary points we obtain a 3-D surface mesh which is used by Tetgen (Si 2003) to create the 3-D mesh. As a result, a tetrahedral mesh of 79 611 nodes is created which reflects Merapi's surface topography to a high degree. Fig. 8(b) shows the mesh of Merapi's northern slope and the position of the electrodes used (bullets). The size of the tetrahedrons is small close to the profile (1 m) and grows larger with distance such that the whole volcano can be simulated at affordable cost.
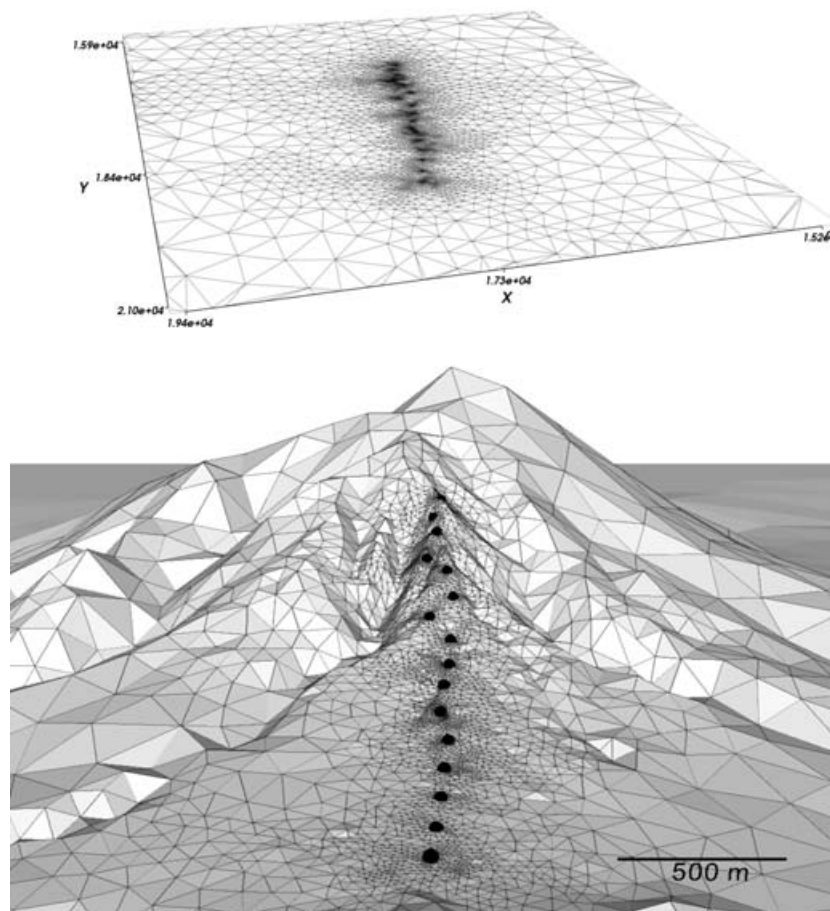
Figure 8. (a) Section of the 2-D mesh with local refinement at vicinity of electrodes, (b) 3-D surface mesh with topography at the northern slope of Merapi volcano, the dots represent the location of electrodes.
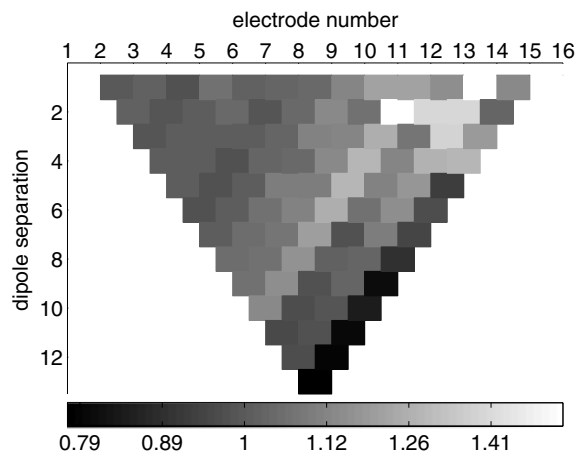
Figure 9. Dipole–dipole pseudo-section of the topography effect *t* along the profile at the northern slope of Merapi volcano. The origin is at the foot of the mountain. The abscissa denotes the electrode number, the ordinate reflects the dipole separation. The individual values are plotted in the centre between the two dipoles involved.

The use of quadratic shape function yields a mesh with 566 736 nodes. Fig. 9 shows the resulting pseudo-section of the topography effect. On the left (electrodes 1–10), we see the expected half-space values of around $t = 1$ since the topography on the lowest part of the profile is almost plane. Close to the upper right-hand side corner an increase of the resistivities up to 50 per cent can be observed. Since the current lines are compressed by the valleys running parallel to the electrode line we yield increased voltages and, thus, increased apparent resistivities. All readings associated with the last dipole (electrodes 15 and 16), that is, on a diagonal line from the upper right-hand side corner of the pseudo-section to the lower central value, are decreased by 20 per cent. This may be caused by the steep dip of the dipole axis toward the top of the volcano, since the last electrode is situated on top of a narrow ridge.

The potentials for a homogeneous conductivity can be used to determine the geometric factors. Thus, the resulting apparent resistivities contain only the effect of the subsurface. Having calculated the primary potential we may now simulate the potentials for arbitrary conductivity distributions using the SP technique on a relatively coarse grid. See Günther *et al.* (2006) for further examples and its use in the inversion.

Note that the potentials at the electrodes may also be obtained by the boundary element method (Xu 2001). This results in solving a dense system of equations where the degree of freedoms equals the number of nodes in the surface mesh. This may be more efficient in some cases. However, to solve for the SP, we need the potential in the interior, which can only be achieved by numerical integration for each node representing a large effort.

5 COMPUTATIONAL ASPECTS

Now, we review the meshes of the previous sections with respect to solving the system of equations. For iterative methods, a stopping

Table 1. Mesh sizes and number of non-zeros (nnz) in the stiffness matrix for the four meshes in the preceding examples.

Example	Half-sphere	Half-space	Gallery	Merapi
Nodes	1769	38 533	128 169	566 736
nnz	24 427	542 459	$1.86 \cdot 10^6$	$7.74 \cdot 10^6$

Table 2. Computation time t and number of non-zero entries (nnz) for the Cholesky factor and different reordering strategies (half-sphere).

Reordering	None	RCM	MMD	AMD
t(Chol)	1.85 s	0.06 s	0.09 s	0.09 s
nnz(Chol)	750 238	181 299	150 454	119 843

criterion has to be defined depending on the accuracy of the solution. In our experience a relative residual value of 10^{-6} is sufficient for practical purposes and is used in all computations. Table 1 gives an overview of the size of the models used in the last two sections. The node numbers span a range of almost four orders in magnitude.

Proceeding in the order of the mesh size we start with the small-scale problem of the conducting sphere with 1769 nodes and 21 right-hand side vectors. The stiffness matrix contains 24 427 non-zero entries which is $\approx$14 per row. Due to the small size, a direct equation solver is appropriate. Once the factorization is done the back-substitutions for the individual sources are obtained almost instantly. The Cholesky factor is computed in 1.85 s and contains 750 238 non-zero elements, which need about 11.5 MB memory if 12 bytes/entry are considered.

In order to reduce the amount of storage, reordering of the matrix rows and columns is performed in such a way that the number of non-zeros (nnz) in the Cholesky factor is minimized. In Table 2 different reordering strategies are compared: RCM, MMD and AMD (see Section 2.3).

We see that all methods can reduce the nnz drastically, also the computing time is decreased by several decades. AMD performs best with a reduction factor of about 6. In Fig. 10 the sparsity structure is shown for the original and reordered stiffness matrix. We

see that the neighbouring relations of the first elements are changed such that the according entries are located near the main diagonal.

The locally refined homogeneous half-space with quadratic shape functions (38 533 nodes) still represents a moderate mesh with a stiffness matrix **A** of 542 459 non-zero elements. Without reordering, the Cholesky factor obtains $6.84 \cdot 10^8$ elements corresponding to 780 MB RAM which almost exceeds the memory limits of a current standard PC (1 GB). However, with AMD reordering the allocation can be reduced to nnz $= 1.07 \cdot 10^7$ or 120 MB. Due to this great benefit we use the AMD reordering technique for all examples.

The next largest problem is the gallery (128 169 nodes, 1.8 Mio nnz's in **A**) with 50 electrodes. The (reordered) Cholesky factor obtains $6.38 \cdot 10^7$ nnz's or 730 MB. On our PC's with 1 GB memory, 200 000 nodes represent the upper limit for direct equation solvers. The algorithm implemented in the TAUCS package (Toledo *et al.* 2001) needs about 3 s for the symbolic analysis and 52 s for the multifrontal factorization. The following back-substitutions are carried out in 111 s which is about 2 s for each electrode.

The Merapi mesh with 566 736 degrees of freedom cannot be solved with direct methods due to memory limitations. Hence, we use conjugate gradient methods for solving the system of equations. Nevertheless, it is worth to carefully choose the pre-conditioner since the system is solved for each of the 16 electrodes. We choose IC pre-conditioning as used by Li & Spitzer (2002) and regard both variants (IC-nofill and IC-droptol, see Section 2.3) with different thresholds. As for the complete factorization, the nnz can be drastically reduced by AMD reordering. Table 3 shows the computer resources used for various threshold values. The number of iterations and the run time can be decreased by a finer threshold. However, the memory requirements grow. We expect an increase of run time for even smaller values than 10^{-4}, because the back-substitution requires more time for a greater nnz (Günther 2004).

To summarize, the numerical computations must always find a trade-off between the resources speed and memory. Mesh size and available computer memory determine the speed of the solvers. Direct methods should be used whenever it is affordable. Conjugate gradient methods with IC pre-conditioners are the alternative for most cases. The threshold value of the incomplete factorization must
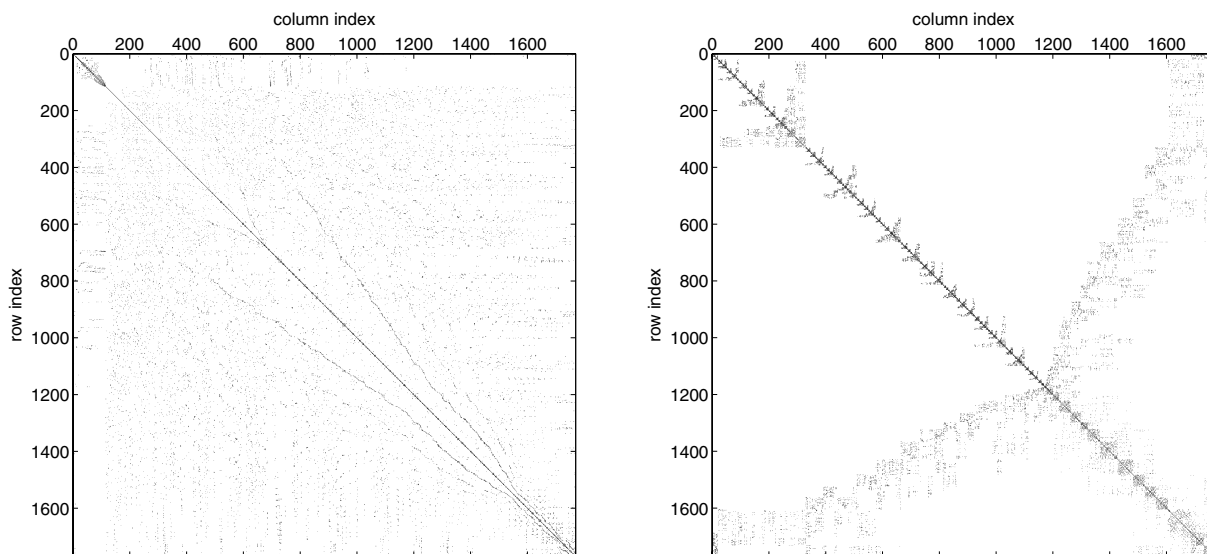
Figure 10. Sparsity structure of the original (left) and AMD-reordered (right) stiffness matrix for the mesh of the sphere model. The non-zero entries (denoted by dots) show a much tighter band width after reordering.

Table 3. Computing time t, memory requirements and number of iterations of the ICCG method for different pre-conditioners (Merapi mesh with 16 source vectors).

Thresh.	Time(IC)	Memory	Iter.	t/Iter	Total t
nofill	201 s	104 MB	146	1.6 s	65.1 min
10^{-1}	140 s	89 MB	170	1.6 s	74.8 min
10^{-2}	144 s	120 MB	94	1.8 s	47.7 min
10^{-3}	180 s	266 MB	45	2.9 s	37.9 min
10^{-4}	393 s	561 MB	19	5.5 s	34.8 min

be chosen carefully to meet memory limits and to minimize calculation time. For very large meshes, the SSOR pre-conditioner is advantageous since it allows pre-conditioning without additional storage (Spitzer 1995). However, convergence becomes slower.

6 DISCUSSION AND CONCLUSIONS

In this paper we have addressed the simulation of dc resistivity data with finite elements. Special attention has been paid to the incorporation of 3-D surface and subsurface topography. For this reason unstructured tetrahedral meshes provide the highest flexibility for describing arbitrary model geometries. The derived geometry effect helps to understand how the physical fields are affected by the geometry of the modelling domain.

We have distinguished between two techniques, the simulation of the total potential and secondary potential. By the latter, accurate simulations can be carried out using small-scale meshes. The main computational effort is associated with the simulation of the primary potential. However, for all problems with more than one source, that is, more than one forward run we gain efficiency by exploiting the SP. This is especially advantageous for the inverse problem.

Whereas the SP can be obtained on a relatively coarse mesh, an accurate simulation of the TP requires a distinct mesh refinement. We suggest a local spatial refinement in the vicinity of the electrodes (at least 1/10 electrode spacing) in combination with the global use of quadratic shape functions. A further improvement of efficiency may be achieved by adaptive mesh refinement using an *a posteriori* error estimator (Verführt 1996). The question remains whether the geometry effect may be calculated more efficiently with the boundary element method (Xu *et al.* 1988).

For the solution of the arising systems of equations we propose two ways: Small-scale problems are most efficiently solved by direct multifrontal solvers. This is the case for all simulations of the SP. Regarding larger systems of equations, as arising primarily from TP simulations, conjugate gradient methods with IC pre-conditioners are the method of choice. The trade-off depends mainly on the available computer memory to store the Cholesky factor of the matrix. Matrix reordering techniques help to reduce memory requirements drastically.

With the presented techniques it is possible to simulate complicated geometries and conductivity distributions within short time on standard computers. Hence, the way to 3-D inversion with arbitrary topography has been opened up and will be considered in a following paper (Günther *et al.* 2006).

ACKNOWLEDGMENTS

REFERENCES

Amestoy, P.R., Davis, T.A. & Duff, I.S., 1996. An approximate minimum degree ordering algorithm, *SIAM Journal on Matrix Analysis and Applications,* **17**(4), 886–905.

Coggon, J.H., 1971. Electromagnetic and electrical modeling by the finite element method, *Geophysics,* **36,** 132–155.

Davis, T.A., Gilbert, J.R., Larimore, S.I. & Ng, E.G., 2000. A column approximate minimum degree ordering algorithm, Tech. Rep. TR-00-005, Department of Computer and Information Science and Engineering, University of Florida.

Dey, A. & Morrison, H.F., 1979. Resistivity modeling for arbitrarily shaped three-dimensional structures, *Geophysics,* **44**(4), 753–780.

Dieter, K., Paterson, N.R. & Grant, F.S., 1969. IP and resistivity type curves for three-dimensional bodies, *Geophysics,* **34,** 615–632.

Duff, I.S., Erisman, A.M. & Reid, J.K., 1986. *Direct Methods for Sparse Matrices*, Clarendon Press, Oxford.

Fox, R.C., Hohmann, G.W., Killpack, T.J. & Rijo, L., 1980. Topographic effects in resistivity and induced-polarization surveys, *Geophysics,* **45**(1), 75–93.

Friedel, S., Brunner, I., Jacobs, F. & Rücker, C., 2000. New results from DC resistivity imaging along the flanks of Merapi volcano, in *Decade-Volcanoes Under Investigation*, pp. 23–29, eds Buttkus, B., Greinwald, S. & Ostwald, J., Mitteilungen der Deutschen Geophysikalischen Gesellschaft, Sonderband IV/2000, Deutsche Geophysikalische Gesellschaft.

Günther, T., 2004. Inversion Methods and Resolution Analysis for the 2D/3D Reconstruction of Resistivity Structures from DC Measurements, *PhD thesis,* Freiberg University of Mining and Technology, available from `http://fridolin.tu-freiberg.de`.

Günther, T., Rücker, C. & Spitzer, K., 2006. Three-dimensional modeling and inversion of dc resistivity data incorporating topography – II. Inversion, *Geophys. J. Int.*, doi:10.1111/j.1365-246X.2006.03011.x (this issue).

Hestenes, C.M.R. & Stiefel, E., 1952. Methods of conjugate gradients for solving linear systems, *J. Res. Nat. Bur. Stand,* **49,** 409–436.

Holcombe, H.T. & Jiracek, G.R., 1984. Three-dimensional terrain corrections in resistivity surveys, *Geophysics,* **45,** 75–93.

Karypis, G. & Kumar, V., 1998. A fast and high quality multilevel scheme for partitioning irregular graphs, *SIAM Journal on Scientific Computing,* **20**(1), 359–392.

Kershaw, D.S., 1978. The incomplete Cholesky-conjugate gradient method for the iterative solution of systems of linear equations, *J. Comput. Phys.,* **26,** 43–65.

Large, D.B., 1971. Electrical potential near a spherical body in a conducting half-space, *Geophysics,* **36,** 763–767.

Li, Y. & Spitzer, K., 2002. Three-dimensional dc resistivity forward modelling using finite elements in comparison with finite-difference solutions, *Geophys. J. Int.,* **151,** 924–934.

Loke, M.H. & Barker, R.D., 1996. Practical techniques for 3d resistivity surveys and data inversion, *Geophys. Prospect.,* **44,** 499–523.

Lowry, T., Allen, M.B. & Shive, P.N., 1989. Singularity removal: a refinement of resistivity modeling techniques, *Geophysics,* **54**(6), 766–774.

Mufti, I.R., 1976. Finite-difference resistivity modeling for arbitrarily shaped two-dimensional structures, *Geophysics,* **41,** 62–78.

Okabe, M., 1981. Boundary element method for the arbitrary inhomogeneities problem in electrical prospecting, *Geophys. Prospect.,* **29,** 39–59.

Pain, C.C., Herwanger, J.V., Saunders, J.H., Worthington, M.H. & de Oliviera, C.R.E., 2003. Anisotropic resistivity inversion, *Inverse Problems,* **19,** 1081–1111.

Pridmore, D.F., Hohmann, G.W., Ward, S.H. & Sill, W.R., 1980. An investigation of finite-element modelling for electrical and electromagnetical data in three dimensions, *Geophysics,* **46,** 1009–1024.

Queralt, P., Pous, J. & Marcuello, A., 1991. 2-d resistivity modeling: an approach to arrays parallel to the strike direction, *Geophysics,* **56**(7), 941–950.

Saad, Y., 1996. *Iterative Methods for Sparse Linear Systems,* PWS, Boston.

Sasaki, Y., 1994. 3-d resistivity inversion using the finite-element method, *Geophysics,* **59**(12), 1839–1848.

Shewchuk, J.R., 1998. Tetrahedral mesh generation by delaunay refinement, in *Proceedings of the Fourteenth Annual Symposium on Computational Geometry*, pp. 86–95, Association for Computing Machinery, available at http://www.cs.cmu.edu/jrs/.

Shewchuk, J.R., 2002. Delaunay refinement algorithms for triangular mesh generation, *Computational Geometry: Theory and Applications,* **22,** 21–74.

Si, H., 2003. TETGEN: a 3d delaunay tetrahedral mesh generator, http://tetgen.berlios.de.

Spitzer, K., 1995. A 3-d finite-difference algorithm for dc resistivity modelling using conjugate gradient methods, *Geophys. J. Int.,* **123,** 903–914.

Spitzer, K. & Wurmstich, B., 1999. Speed and accuracy in 3D resistivity modeling, in *Three-dimensional Electromagnetics*, eds Oristaglio, M. & Spies, B., no. 7 in Geophysical Developments, Society of Exploration Geophysicists.

Toledo, S., Chen, D. & Rothkin, V., 2001. Taucs—a library of sparse linear solvers, http://www.tau.ac.il/ stoledo/taucs/.

Verführt, R., 1996. *A Review of A Posteriori Error Estimation and Adaptive Mesh-Refinement Techniques*, Wiley Teubner, Stuttgart.

Wu, X., Xiao, Y., Qi, C. & Wang, T., 2003. Computations of secondary potential for 3d dc resistivity modelling using an incomplete Choleski conjugate-gradient method, *Geophys. Prospect.,* **51,** 567.

Xu, S.Z., 2001. *The boundary element method in geophysics*, Geophysical monograph series, Society of exploration geophysics.

Xu, S.Z., Gao, Z.C. & Zhao, S.K., 1988. An integral formulation for 3-D terrain modeling for resistivity surveys, *Geophysics,* **53,** 564–552.

Yi, M.-J., Kim, J.-H., Song, Y., Cho, S.-J., Chung, S.-H. & Suh, J.-H., 2001. Three-dimensional imaging of subsurface structures using resistivity data, *Geophys. Prospect.,* **49**(4), 483–497.

Zhang, J., Mackie, R.L. & Madden, T.R., 1995. 3-d resistivity forward modeling and inversion using conjugate gradients, *Geophysics,* **60**(5), 1313–1325.

Zhao, S. & Yedlin, M.J., 1996. Some refinements on the finite-difference method for 3-d dc resistivity modeling, *Geophysics,* **61**(5), 1301–1307.

Zhdanov, M.S. & Keller, G.V., 1994. *The Geoelectrical Methods in Geophysical Exploration*, Methods in Geochemistry and Geophysics, Elsevier, Amsterdam, London, New York, Tokyo.

Zhou, B. & Greenhalgh, S.A., 2001. Finite element three-dimensional direct current resistivity modelling: accuracy and efficiency considerations, *Geophys. J. Int.,* **145,** 679–688.

Zienkiewicz, O.C., 1977. *The Finite Element Method*, McGraw-Hill, London, 3rd edn.

APPENDIX A: ELEMENT INTEGRATION AND SHAPE FUNCTIONS

The approximate solution u_h for the continuous potential $u \approx u_h(x_n, y_n, z_n)$ is represented by discrete points (nodes) (x_n, y_n, z_n), $n = 1, \ldots, N$. By using polynomial shape functions N_n we transform the continuous approximate solution into a discrete vector of unknown coefficients $\mathbf{u} \in \mathrm{I\!R}^N$ with

$$u \approx u_h = \sum_{n=1}^{N} N_n(x, y, z) u_n. \tag{A1}$$

Domain and boundary are discretized into sub-domains $\Omega^{(i)}$ and boundary elements $\Gamma^{(i)}$. The application of (A1) on (2) yields with the Galerkin method ($w_i = N_i$) the FE formulation

$$\sum_{k=1}^{N} \left(\int_\Omega \sigma \nabla N_k \cdot \nabla N_l \, d\Omega + \int_\Gamma \sigma \alpha N_k N_l \, d\Gamma \right) \mathbf{u} =$$
$$\sum_{i=1}^{E} \int_\Omega N_k I \delta(\mathbf{r} - \mathbf{r}_s) \, d\Omega + \sum_{i=1}^{B} \int_\Gamma N_k I \delta(\mathbf{r} - \mathbf{r}_s) \, d\Gamma, \tag{A2}$$

represented by the system of equations $\mathbf{Au} = \mathbf{b}$ with $\mathbf{A} = \sum_{i=1}^{E} \mathbf{A}^{(i)} + \sum_{i=1}^{B} \mathbf{B}^{(i)}$ and the element matrices

$$A_{k,l}^{(i)} = \int_{\Omega^{(i)}} \sigma_i \nabla N_k \cdot \nabla N_l \, d\Omega \quad \text{and} \tag{A3a}$$

$$B_{k,l}^{(i)} = \int_{\Gamma^{(i)}} \sigma_i \alpha N_k N_l \, d\Gamma \quad \text{for} \quad k, l = 1 \ldots N. \tag{A3b}$$

For a source position $\mathbf{r}_s$ the individual entries for the right-hand side in (A2) are determined by

$$b_k = \sum_{i=1}^{E} \int_{\Omega^{(i)}} N_k I \delta(\mathbf{r} - \mathbf{r}_s) \, d\Omega + \sum_{i=1}^{B} \int_{\Gamma^{(i)}} N_k I \delta(\mathbf{r} - \mathbf{r}_s) \, d\Gamma. \tag{A3c}$$

The choice of shape functions determines the quality of the approximated potential. Shape functions can easily be formed by transforming the Cartesian coordinates (x_i, y_i, z_i) into natural (or element) coordinates (ζ_i). For an edge ($\mathrm{I\!R}^1$) defined by two nodes $P_1(x_1)$ and $P_2(x_2)$ the relations are

$$x = x_1 \zeta_1 + x_2 \zeta_2 \quad \text{and} \quad \zeta_1 + \zeta_2 = 1,$$
$$\text{such that} \quad \zeta_1 = \frac{x_2 - x}{x_2 - x_1} \quad \text{and} \quad \zeta_2 = \frac{x - x_1}{x_2 - x_1}. \tag{A4}$$

The linear shape functions for the natural elements (edge, triangle, tetrahedron) equal the natural coordinates ($N_i = \zeta_i$). Hence the load vector entries for an edge are

$$\mathbf{b}_{P_1} = \int_0^1 \zeta_1(x) I \delta(x - x_s) \, dx = \zeta_1(x_s) = \frac{x_2 - x_s}{x_2 - x_1}$$
$$\mathbf{b}_{P_2} = \int_0^1 \zeta_2(x) I \delta(x - x_s) \, dx = \zeta_2(x_s) = \frac{x_s - x_1}{x_2 - x_1}. \tag{A5}$$

If the source position is located on one of the nodes, the particular entry is 1. If not, both yield entries. The same procedure also holds for a face or an element. Thus a node-independent electrode positioning can be achieved for TP calculations.

In order to use quadratic shape functions we need an additional node at the edge centre and the three shape functions

$$N_1 = \zeta_1(2\zeta_1 - 1), \quad N_2 = \zeta_2(2\zeta_2 - 1), \quad N_3 = 4\zeta_1 \zeta_2. \tag{A6}$$

The integration of $\mathbf{b}$ works analogously.

For a triangle ($\mathrm{I\!R}^2$) with the nodes $P_1(x_1, y_1)$, $P_2(x_2, y_2)$ and $P_3(x_3, y_3)$ the relation between Cartesian and natural coordinates is given by

$$x = x_1 \zeta_1 + x_2 \zeta_2 + x_3 \zeta_3$$
$$y = y_1 \zeta_1 + y_2 \zeta_2 + y_3 \zeta_3. \tag{A7}$$

Considering $\zeta_1 + \zeta_2 + \zeta_3 = 1$ we yield

$$\zeta_1 = \frac{1}{J} \left((x_2 y_3 - x_3 y_2) + x(y_2 - y_3) + y(x_3 - x_2) \right)$$

$$\zeta_2 = \frac{1}{J} \left((x_3 y_1 - x_1 y_3) + x(y_3 - y_1) + y(x_1 - x_3) \right)$$

$$\zeta_3 = \frac{1}{J} \left((x_1 y_2 - x_2 y_1) + x(y_1 - y_2) + y(x_2 - x_1) \right) \quad \text{with}$$

$$J = (x_2 - x_1)(y_3 - y_1) - (x_3 - x_1)(y_2 - y_1).$$

J is called Jacobian determinant and equals the doubled triangle area. As for the edge the linear shape functions are $N_i = \zeta_i$. The quadratic shape functions read

$$N_i = \zeta_i(2\zeta_i - 1) \quad \text{for} \quad i = 1 \ldots 4$$

$$N_4 = \zeta_1\zeta_2, \quad N_5 = \zeta_2\zeta_3, \quad N_6 = \zeta_3\zeta_1. \tag{A8}$$

The natural coordinates for a tetrahedron ($\mathbb{R}^3$) are obtained similar to eqs (A4) and (A7) by solving

$$\begin{pmatrix} 1 \\ x \\ y \\ z \end{pmatrix} = \begin{pmatrix} 1 & 1 & 1 & 1 \\ x_1 & x_2 & x_3 & x_4 \\ y_1 & y_2 & y_3 & y_4 \\ z_1 & z_2 & z_3 & z_4 \end{pmatrix} \begin{pmatrix} \zeta_1 \\ \zeta_2 \\ \zeta_3 \\ \zeta_4 \end{pmatrix}. \tag{A9}$$

The linear shape functions are again $N_i = \zeta_i$ whereas the quadratic ones read

$$N_i = \zeta_i(2\zeta_i - 1) \quad \text{for} \quad i = 1 \ldots 4$$

$$N_5 = 4\zeta_1\zeta_2, \quad N_6 = 4\zeta_2\zeta_3, \quad N_7 = 4\zeta_3\zeta_1$$

$$N_8 = 4\zeta_1\zeta_4, \quad N_9 = 4\zeta_2\zeta_4, \quad N_{10} = 4\zeta_3\zeta_4. \tag{A10}$$

To obtain the right-hand side of (A3a) we need to integrate over the boundary triangles by using the natural coordinates (A7) and the corresponding shape functions. Zienkiewicz (1977) provides integral formulas with arbitrary powers a, b, and c on triangles,

$$\int_{\Omega^{(i)}} \zeta_1^a \zeta_2^b \zeta_3^c \, dx \, dy = \frac{a!b!c!}{(a+b+c+2)!} J, \tag{A11}$$

and tetrahedrons,

$$\int_{\Omega^{(i)}} \zeta_1^a \zeta_2^b \zeta_3^c \zeta_4^d \, dx \, dy \, dz = \frac{a!b!c!d!}{(a+b+c+d+3)!} 6V, \tag{A12}$$

where V is the tetrahedral volume. For the domain integral we need to differentiate the ζ_i with respect to the natural coordinates. By inserting the resulting powers as $a/b/c$ into eq. (A11) the element matrix is constructed.